Journal of Power Sources 182 (2008) 389–399

Contents lists available at ScienceDirect

Journal of Power Sources

journal homepage: www.elsevier.com/locate/jpowsour

Ageing of anode-supported solid oxide fuel cell stacks including thermal cycling, and expansion behaviour of MgO–NiO anodes

J. Van herle[a,*], D. Perednis[b], K. Nakamura[c], S. Diethelm[d], M. Zahid[b], A. Aslanides[b], T. Somekawa[c], Y. Baba[c], K. Horiuchi[c], Y. Matsuzaki[c], M. Yoshimoto[e], O. Bucheli[d]

[a] *Laboratory of Industrial Energy Systems (LENI), Faculty of Engineering (STI), Ecole Polytechnique Fédérale de Lausanne (EPFL), Station 9, CH-1015 Lausanne, Switzerland*
[b] *European Institute for Energy Research (EIFER), Emmy-Noether-Straße 11, D-76131 Karlsruhe, Germany*
[c] *Product Development Department, Tokyo Gas Co. Ltd., 3-13-1 Minamisenju, Arakawa-ku, Tokyo 116-0003, Japan*
[d] *HTceramix SA, 26 Avenue des Sports, CH-1400 Yverdon-les-Bains, Switzerland*
[e] *Department of Innovative and Engineered Materials, Interdisciplinary Graduate School of Science and Engineering, Tokyo Institute of Technology, 4259-J2-46 Nagatsuta, Midori-ku, Yokohama 226-8503, Japan*

ARTICLE INFO

Article history:
Received 20 February 2008
Received in revised form 29 February 2008
Accepted 4 March 2008
Available online 18 March 2008

Keywords:
Anode-supported SOFC
Ageing
Thermal cycling
Nickel anode expansion
(Mg, Ni)O solid solution

ABSTRACT

This paper reports on medium term tests of anode-supported five-cell short stacks, as well as on some separate anode development. Two stacks were operated under steady-state conditions: one with unprotected metal interconnects, H_2 fuel and 0.35 A cm^{-2} (40% fuel utilisation) polarisation current showed an average cell voltage degradation of 56 mV per 1000 h for 2750 h; one with coated metal interconnects, synthetic reformate fuel and 0.5 A cm^{-2} (60% fuel utilisation) polarisation current showed an averaged cell voltage degradation slope of 6.6 mV per 1000 h for 800 h before a power cut prematurely interrupted the test. A third stack was subjected to 13 complete thermal cycles over 1000 h, average cell voltage degradation was evaluated to −2 mV per cycle for operation at 0.3 A cm^{-2}, open circuit voltage (OCV) remained stable, whereas area specific resistance (ASR) increase amounted on average to 0.008 Ω cm^2 per cycle.

To improve anode reoxidation tolerance, MgO addition was considered. (Mg, Ni)O solid solutions were synthesized from MgO and NiO powders at 1500 °C for 2 h in air. Samples were reduced at 1000 °C in 4 vol% H_2 in N_2, and their expansion behaviour was observed. XRD and SEM/EDX analysis suggested that the expansion was caused by the segregation of Ni particles between (Mg, Ni)O grains.

1. Introduction

Solid oxide fuel cells (SOFC) require to demonstrate durability both under steady-state operation and transient operation (load and temperature cycling). For steady-state stability, protective coating on the air side of FeCr steel interconnects is one of the decisive measures, in order to limit important degradation rates due to chromium poisoning of the cathode–electrolyte interface. With respect to transient operation, it is estimated that a SOFC system product needs to cope with at least 10–15 full thermal cycles per year, with a tolerable loss well below 1% per cycle.

In the "Real-SOFC" project (6th Framework Programme of the European Commission, contract SES6-CT-2003-502612), a series of tests on state-of-the-art SOFC short stacks (typically five cells) have been conducted by several European partners. The used stack concept in this paper is that of HTceramix SA (Switzerland), capable of integrating cells not only of own produce but also from project partners such as the Energy Research Center ECN (NL), Haldor Topsø AS (DK), or the Research Center Jülich FZJ (D). The design is so-called "first generation R-configuration", Fig. 1, consisting of 80 mm × 80 mm square cells (anode-supported electrolyte cells, ASE) with internal feed holes for fuel and air, 50 cm^2 active cathode area, and 0.5–1 mm thick unprofiled FeCr interconnect sheets [1].

This paper is composed of three parts. The first reports on medium-term steady-state operation (1000–3000 h) of two 5-cell stacks with and without protective interconnect coating, using reputedly stable ASE cells from Haldor Topsø and ECN. The second reports on thermal cycling of a 5-cell stack (1000 h, 13 cycles) using ECN cells, and includes other transient behaviour results (performance activation with current load increase). Interconnects were not coated in this latter test, the influence of which was regarded as minor, since the effective duration of operation at high temperature remained short (ca. 420 h).

* Corresponding author. Tel.: +41 21 693 35 10; fax: +41 21 693 35 02.
E-mail addresses: jan.vanherle@epfl.ch (J. Van herle), kzo_naka@tokyo-gas.co.jp (K. Nakamura), mohsine.zahid@eifer.uni-karlsruhe.de (M. Zahid), olivier.bucheli@htceramix.ch (O. Bucheli).

0378-7753/$ – see front matter © 2008 Elsevier B.V. All rights reserved.
doi:10.1016/j.jpowsour.2008.03.006

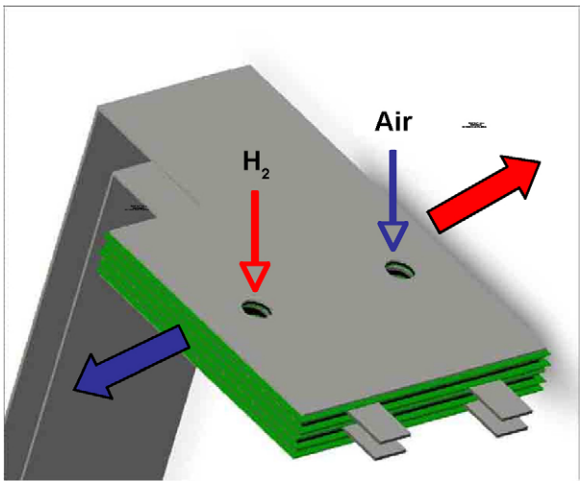

Fig. 1. Sketch of 5-cell stack with gas feed holes, interconnects with latches for attaching potential leads, and current collection end plates.

Both material-intrinsic and design-parameter aspects including operating conditions contribute to overall degradation [2–5]. With planar anode-supported cell geometry, protection of the anode against reoxidation is paramount, as will be confirmed from the thermal cycling test.

One interesting way to counteract the anode expansion upon reoxidation is the addition of MgO. MgO-added anodes expand during reduction and shrink during reoxidation. This approach, developed and studied by colleagues from Tokyo Gas and Tokyo Institute of Technology, forms the third part of the paper. Ni/MgO is known for superior properties and coking resistance during steam reforming [6,7]. Because the active catalyst is obtained by reduction of a (Mg, Ni)O solid solution without the necessity of producing and dispersing fine Ni particles, it is considered to be simple and low cost. By applying it to SOFCs, internal reforming is possible at high temperature [8]. Recently, segmented-in-series type SOFC achieved an efficiency of 56.1% (LHV) using methane fuel [9]. Of particular interest in this study was the redox behaviour of (Mg, Ni)O solid solutions.

2. Experimental

Assembly and testing of HTceramix 5-cell R-design stacks has been reported several times before [2,3,10]. Summarised, ASE cells of the geometry shown in Fig. 1 are sandwiched between flat interconnect sheets of the same size and shape, using intercalation layers (SOFConnex^{TM}) for gas distribution and current collection. Sealing is accomplished around holes and along borders with rings and strips from mica-like or vermicullite materials. Cells were delivered by ECN and Haldor Topsø and consist of Ni-YSZ anode supports with thin 8YSZ electrolyte and $LaSrMnO_3$–8YSZ cathodes (Haldor Topsø, ECN "ASC1" cells) or $LaSrFeCo_3$ cathodes (ECN "ASC2" cells), including a ceria compatibility layer in the second case. Stack current is collected on the interconnect end plates extending out of the hot zone controlled by a furnace. Repeat element voltages are measured between every successive interconnect pair, and temperature by various thermocouples either in contact with the interconnects or placed in gas in/outlet zones. A constant pressure of 0.4 kg cm^{-2} is kept on each stack throughout all testing, via spring loads. At start-up stacks are heated in air, and anodes reduced at high temperature according to cell manufacturer specific protocols.

For steady-state testing, two different 5-cell stacks were operated at 800 °C at the premises of the European Institute for Energy Research (EIFER) in Karlsruhe, Germany. Stack #1 integrated Haldor Topsø ASE cells and 1 mm uncoated CroFer22APU interconnect plates. Stack #2 integrated ECN anode-supported cells with LSFC cathode (ASC2) and 1 mm coated CroFer22APU interconnect plates. A protective coating of $MnCo_{1.9}Fe_{0.1}O_4$ on the interconnect [11] was deposited by atmospheric plasma spraying (APS) at Forschungszentrum Jülich (FZJ). The specifications of both these stacks are listed in Table 1. Testing was carried out using either humidified hydrogen (3% water vapour) or synthetic reformate as fuel (71% H_2, 8% H_2O, 21% CO_2).

For the thermal cycling test, a 5-cell stack #3 using ECN cells with LSM-YSZ cathodes (ASC1) was operated at 800 °C with humidified H_2 fuel (3% H_2O) at EPFL facilities in Lausanne, Switzerland. The heating rate was 180 K h^{-1}, the cooling rate 180 K h^{-1} down to about 500 °C, below which it slowed down and followed the natural cooling curve of the test furnace (Rohde TE Q10, Germany). After the first cycle, heating and cooling was carried out in dilute H_2, typically 50% in N_2, which was reduced to 20% H_2 in N_2 for the cooling phase below 500 °C. At 800 °C, the stack was polarised at constant current (with 0.46 A cm^{-2} for the first six cycles, 0.3 A cm^{-2} afterwards) for typical durations of 24 h, sometimes 40 or 48 h. Forward-scan current–voltage (i–V) characteristics were recorded at the beginning of each cycle, i.e. just after reaching 800 °C at the end of each heating phase, and, unless mentioned otherwise, a backward-

Table 1
Steady-state testing: stack specifications

	Stack #1	Stack #2
Cell manufacturer	Haldor Topsø	ECN
Stack assembly	HTceramix R-design, with SOFConnex between cells and MICs	HTceramix R-design, with SOFConnex between cells and MICs
Interconnect	Crofer 22 APU (1 mm)	Crofer 22 APU (1 mm)
Protective coating	None	$MnCo_{1.9}Fe_{0.1}O_4$ (APS)
Anode	Ni-8YSZ (~300 μm)	Ni-8YSZ (~500 μm)
Electrolyte	8YSZ (10 μm)	8YSZ (5 μm)
Cathode interlayer	No	CYO (3 μm)
Cathode	LSM/8YSZ (20 μm)	LSCF (20–30 μm)
Fuel	H_2 (3% H_2O)	71% H_2, 21% CO_2, 8% H_2O
Air excess ratio	1.6	1.6
Current density	0.35 A cm^{-2}	0.5 A cm^{-2}
Fuel utilisation	40%	60%
Test duration	2750 h	820 h (general power cut)
Average repeat element degradation	6.7% per 1000 h (56 mV kh^{-1})	0.83% per 1000 h (6.6 mV kh^{-1})
Cell 1 (% kh^{-1})	4.3	0.48
Cell 2 (% kh^{-1})	5.3	0.95
Cell 3 (% kh^{-1})	9.9	1.11
Cell 4 (% kh^{-1})	8.8	0.16
Cell 5 (% kh^{-1})	5.6	1.41

Table 2
Test parameter overview of 5-cell stack #3 going through 13 thermal cycles (see also Fig. 7)

Heating	*i–V* scan (fwd/bwd)	Time (h)	*T* (°C) (@ OCV)	OCV (V)	ASR (Ω cm^2)	Load *j* (A cm^{-2})	Load time (h)	Cooling to (°C)
1	F	23	810	0.973	0.492	0.46	24	
	B	48			n.d.[a]			140
2	F	69	800	0.982	0.567	0.46	24	
	B	94	806	0.970	0.527			25
3	F	165	810	0.978	0.564	0.46	24	
	B	190	804	0.973	0.554			141
4	F	215	810	0.970	0.589	0.4 + 0.46	24 + 24	
	B	263	800	0.973	0.560			23
5	F	335	805	0.984	0.564	0.32 + 0.46	24 + 24	
	B	384	799	0.973	0.563			143
6	F	404	809	0.973	0.545	0.4 + 0.46	20 + 5	
	B	430			n.d.[a]			23
7	F	502	803	0.985	0.614	0 (OCV)	24	
	F	526	801	0.986	0.627	0.3	24	
	B	552	797	0.980	0.566			134
8	F	576	807	0.985	0.645	0.3	24	
	B	601	799	0.976	0.599			123
9	F	670	807	0.982	0.720	0.3	24	
	B	695	800	0.984	0.598			132
10	F	718	810	0.970	0.586	0.28 + 0.3	16 + 24	
	B	760	799	0.971	0.589			25
11	F	841	805	0.984	0.644	0.3	24	
	B	865	799	0.980	0.618			202
12	F	887	804	0.977	0.752	0.24 + 0.3	16 + 24	
	B	930	799	0.974	0.628			23
13	F	1005	807	0.978	0.665	0.3	24	
	B	1032	799	0.973	0.628			135
14	F	1055	805	0.969	0.721	0.3	Cell 3 fails	

OCV and ASR values are averaged over the five cells, and further reported in detail in Figs. 13 and 14. The last column gives the lowest temperature to which the stack was cooled down before the next heating ramp, and the previous two columns the duration and constant current density at which it was operated at 800 °C between thermal cycling.

[a] n.d., not determined.

scan *i–V* was recorded at the end of each current load period, i.e. just before cooling down. An overview of the test sequence for this stack is given in Table 2. Excess airflow in all testing was 1.6. Hydrogen flow in the cycling test was 8 ml min^{-1} cm^{-2}, in the steady-state tests it was 6 ml min^{-1} cm^{-2} or equivalent to that (for reformate).

For synthesizing (Mg, Ni)O solid solutions, starting materials from MgO powder (3.0 μm particle size) and NiO powder (0.7 μm particle size) were prepared in a molar ratio of 65:35. To increase porosity, 20 wt% of pore forming agent (microcrystalline cellulose) was added and mixed together. A solution of poly-vinyl butyral (10 wt% of the mixture) in ethanol was then added, and further mixed at room temperature until the solvent nearly completely evaporated. Finally, the mixed powder was pressed uniaxially into pellets (20 mm diameter) at a pressure of 320 kg cm^{-2}. The pellets were calcined at 1500 °C for 2 h in air to obtain the (Mg, Ni)O solid solution. Their reduction was carried out at 1000 °C in a flow of 4 vol% hydrogen in nitrogen, and the treatments repeated so as to be able to neglect the volume changes of the samples. The expansion behaviour of the samples was determined by measuring the pellet diameters. Scanning electron microscopy (SEM) and energy dispersive X-ray spectroscopy (EDX) were used for analyzing the microstructure and the composition, respectively. X-ray diffraction (XRD) profiles of the powdered samples were measured for phase analysis.

3. Results

3.1. Steady-state testing, with and without interconnect protective coating

Stack #1 was tested for 2750 h at a current load of 0.35 A cm^{-2} (40% fuel utilization) using humidified hydrogen as fuel (Fig. 2). The

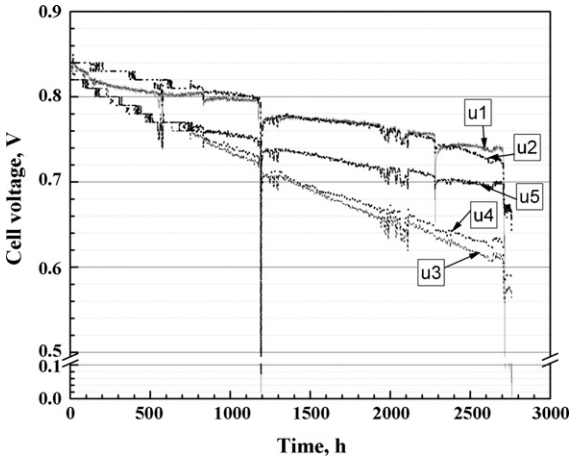

Fig. 2. Repeat element voltage evolution during stack #1 test.

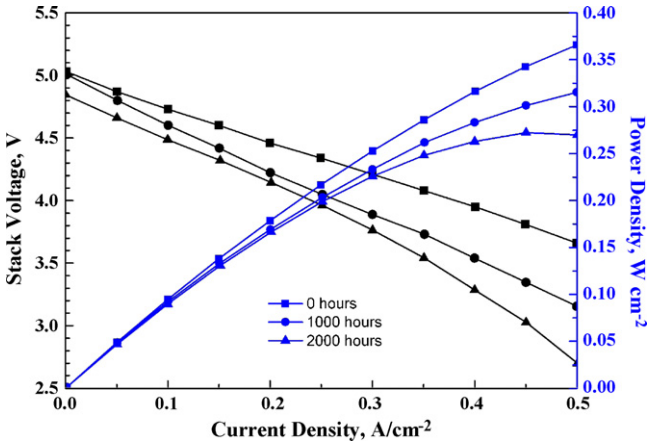

Fig. 3. Current–voltage characteristics of stack #1.

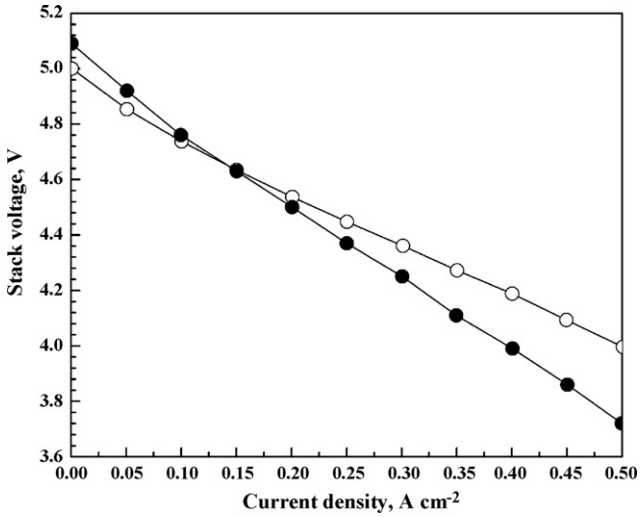

Fig. 5. Initial current–voltage characteristics for both stacks: (●) #1 (ASR = 0.55 Ω cm^2) and (○) #2 (ASR = 0.40 Ω cm^2).

average repeat element ageing rate was 6.7% or 56 mV per 1000 h. Such a degradation of performance can be expected considering the use of uncoated Crofer interconnects [12]. During this test an unforeseen interruption of hydrogen supply (30 min) occurred after 1200 h. The stack recovered to nearly original voltage when hydrogen supply was restored. The best performing repeat element failed suddenly after 2750 h of operation, terminating the test.

Current–voltage (*i*–*V*) measurements were carried out at start-up, after 1000 h and after 2000 h of operation at 800 °C, as given in Fig. 3. Considering area specific resistance (ASR) values at 0.3 A cm^{-2} for reasons further explained below, during the first 1000 h the average ASR increased from 0.52 to 0.72 Ω cm^2. Rate of increase then slowed down to achieve 0.82 Ω cm^2 after 2000 h but the average open circuit voltage (OCV) was lower by ca. 32 mV per cell. This is for one part likely a consequence of the H_2 interruption at 1200 h, and for another part possibly due to deterioration of the compressive seal, as reported elsewhere [5].

Coated Crofer 22 APU interconnects were used in stack #2 to demonstrate the influence of the protective layer on stack ageing. This stack was also operated at more realistic and challenging conditions, increasing current density to 0.5 A cm^{-2} (60% fuel utilization) and using synthetic reformate as fuel instead of hydrogen. Repeat element voltage evolution is plotted in Fig. 4, showing small degradation rates during the 820 h of operation (see Table 1). A direct comparison of both stacks is given at start-up in Fig. 5 and for the first 800 h of operation in Fig. 6. It can of course be argued that both stack tests are little comparable as they contain different cell types. On the other hand, both these cell types are reputed to show intrinsic degradation rates below 1% per 1000 h [13,14]. We therefore believe that the significant difference in stack degradation observed from tests #1 and #2 here can most likely be attributed to the effect of the protective layer.

3.2. Thermal cycling testing

Fig. 7 summarises the cycling test overview. Relevant corresponding values were given in Table 2. A total of 13 cycles (14 heating ramps) was carried out over a total duration of ca. 1060 h. A striking aspect of Fig. 7 is the performance activation taking place systematically at the beginning of each current load period. As will be shown in detail further below, it is more pronounced for one of the border cells (no. 5) and increases with the number of cycles.

Fig. 8A shows the first current–voltage (*i*–*V*) scan taken at 800 °C and 8 ml min^{-1} cm^{-2} of H_2 flow (*t* = 23 h), before steady-state polarisation at 0.46 A cm^{-2} (40% fuel utilisation, u_F). Here the border cell 5 shows a behaviour close to that of the other cells. Average OCV

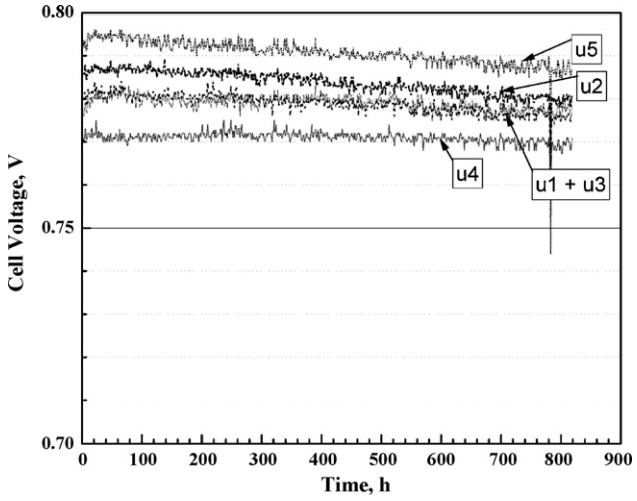

Fig. 4. Repeat element voltage evolution during stack #2 test.

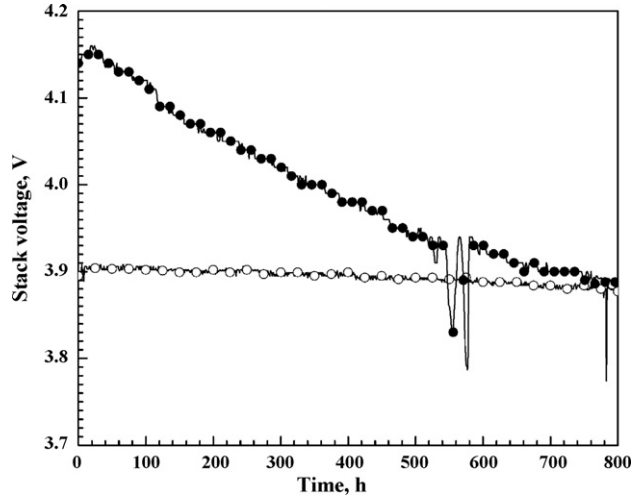

Fig. 6. Comparison of stack voltage evolution: (●) stack #1 (operated at 0.35 A cm^{-2}, 40% u_F); (○) stack #2 (operated at 0.5 A cm^{-2}, 60% u_F).

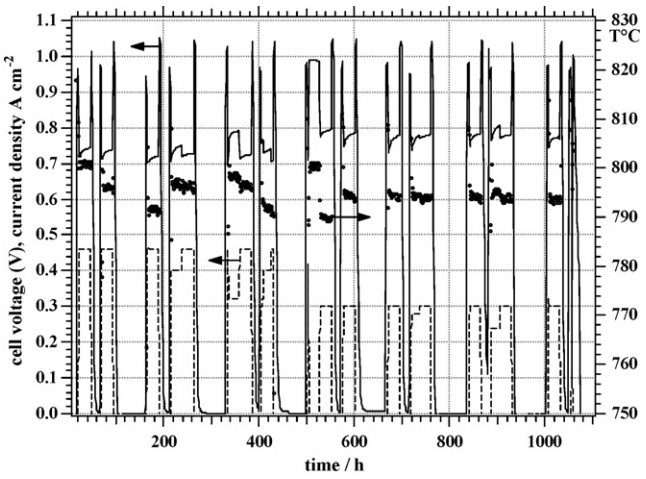

Fig. 7. Thermal cycle test overview of stack #3, showing average repeat element voltage, current density and temperature for the duration of the test.

is low (0.974 V), but not unusual as this was repeatedly observed on other stacks of the same produce. We could show this to originate primarily from seal leakage [5]. Additional factors are due to the finite electronic resistivity of the thin electrolyte leading to a small internal shorting current on the order of 0.01 A cm^{-2} [1,3], and to the anode thickness (0.55 mm) with fairly large open porosity (40%), no sealant being applied on the anode edge facing the internal air feed hole.

ASR values (in Ω cm^2) are given in the graph, approximating the *i*–*V* curves to straight lines with the slopes taken between 0.05 and 0.45 A cm^{-2}. These values are at best only indicative, as further detailed in Fig. 8B, where ASR variation over the current density range is plotted (ASR slopes taken between each pair of neighbouring points of the *i*–*V* curves): clearly "ASR" varies significantly. For further discussion, we chose to compare the average ASR value determined for each curve between 0.2 and 0.3 A cm^{-2}, as it is minimal and fairly constant in this range, and as *i*–*V* recordings in later cycles were not taken beyond 0.3 A cm^{-2} current load (see also Fig. 7).

Fig. 8C, finally, shows performance activation taking place during constant current polarisation (0.46 A cm^{-2}), after recording the *i*–*V* response of Fig. 8A. The activation is visible as voltage increase on each of the five repeat elements, especially for the border cell 5.

We have repeatedly observed and reported such activation behaviour before [10,15]. One effect to consider is the local increase of temperature with current load [16], which we could measure as for example +40 K between OCV and 0.6 A cm^{-2} in separate experiments, where the thermocouple was placed in the intercalation layer close to the electrode–electrolyte interface (within 0.5 mm). The registered temperatures for the present test, plotted along at constant current density of 0.46 A cm^{-2} in Fig. 8C and measured on three interconnects and at both gas inlets, show virtually no variation, though. Activation also takes place over 20 h and more, whereas thermal equilibration is achieved over a few hours at most [17]. The phenomenon is also observed on 1 cm^2 cells, where thermal effects are much smaller than in stacks [16]. The other border cell (no. 1), which is certainly permanently colder than the center cells (cf. its higher OCV) because of cooling via the test flange in contact with it, still shows activation as well.

This performance increase consistently tends to be more pronounced with the least performing cell. Therefore at least another process than only local heating seems at work. Noponen et al. [18], using similar stacks as tested here, also within the "Real-SOFC" project, suggested a correlation with cathode behaviour, which

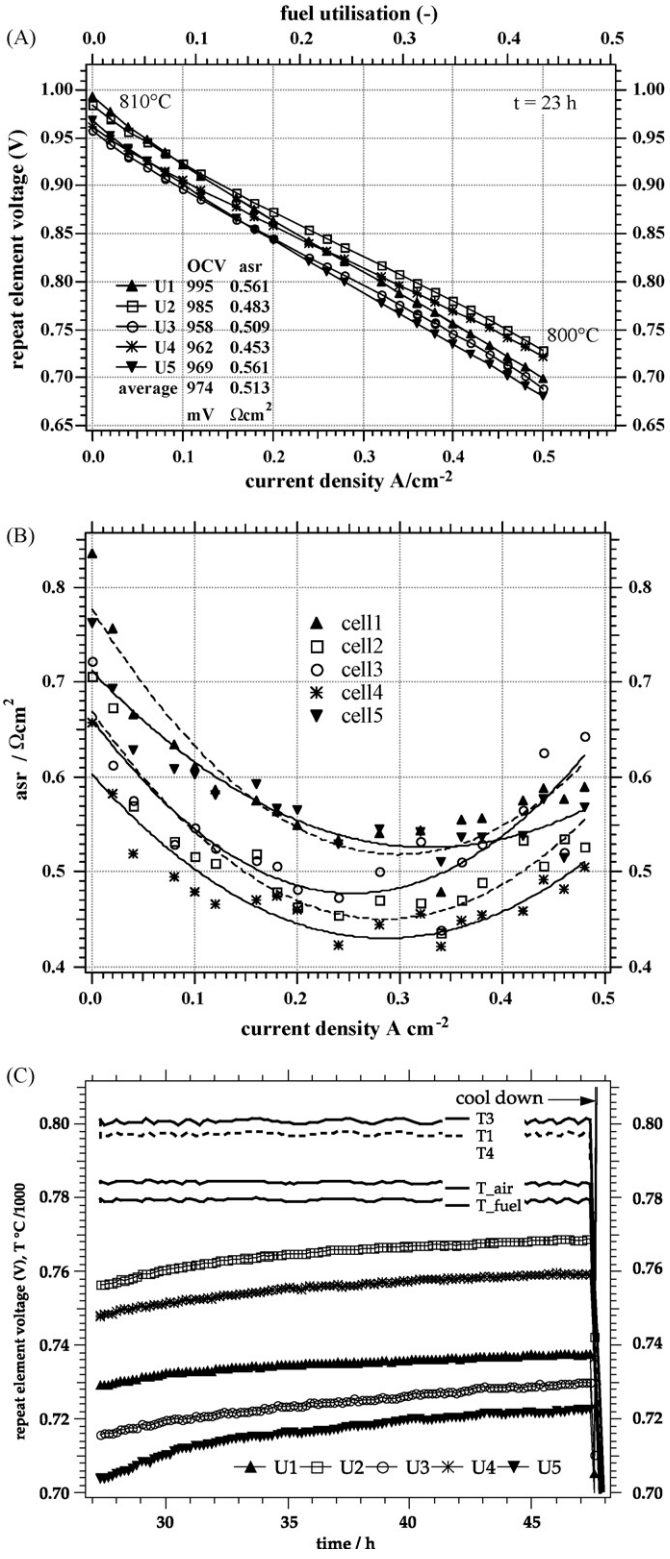

Fig. 8. (A) Current–voltage output of 5-cell stack #3 at beginning of thermal cycle test. (B) ASR evolution as a function of current density for *i*–*V* output plotted in (A). (C) Voltage evolution with time at 0.46 A cm^{-2} stack current, following the *i*–*V* scan shown in (A). Temperature levels during operation are also indicated.

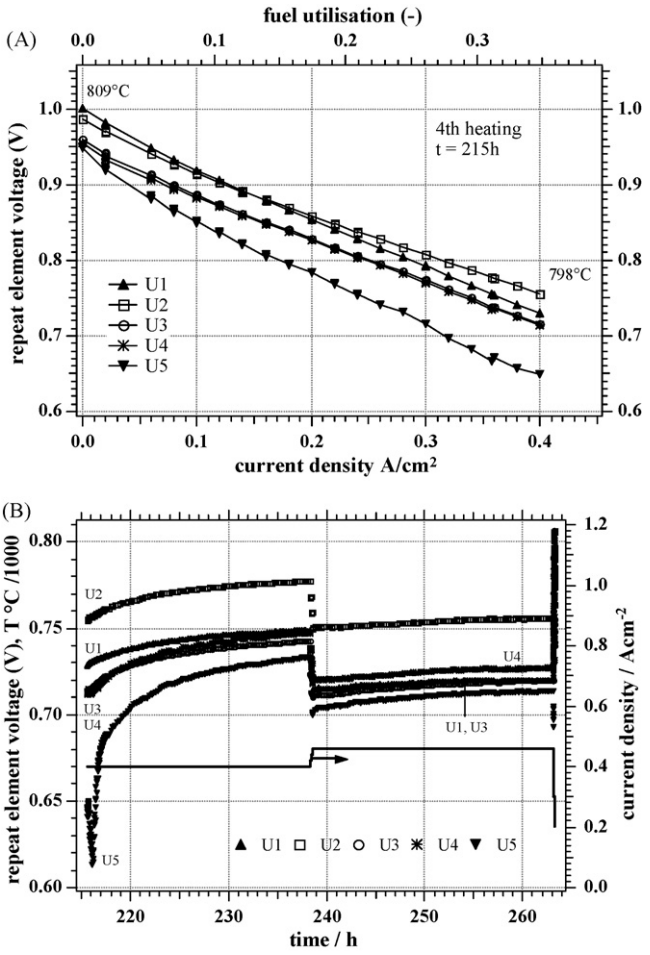

Fig. 9. (A) Current–voltage output of 5-cell stack after the fourth heating (three thermal cycles), showing deviant behaviour of border cell 5. (B) Voltage evolution with time at 0.4 and 0.46 A cm^{-2} stack current, respectively, following the *i*–*V* scan shown in (A).

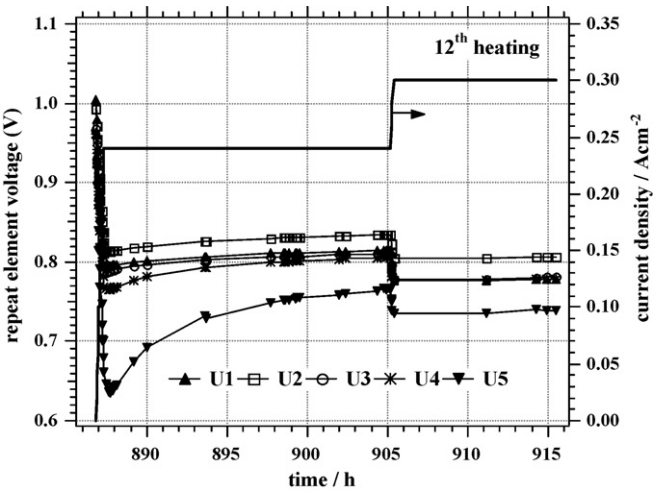

Fig. 10. Voltage evolution with time at 0.24 and 0.3 A cm^{-2} stack current, respectively, following the forward *i*–*V* scan taken at 800 °C at the beginning of the 12th thermal cycle.

becomes gradually more mixed conducting during polarisation. We suggest in our case an influence of the assembly feed, corroborative of their explanation. Gas leakage, in particular as a consequence of poor compressive sealing, is as mentioned fairly important in our test arrangement [5] and not homogeneously distributed over the 5 cells (10 gas compartments), as shown by calculation [4]. Underfed cells then show low-initial output upon repolarisation at the beginning of a load period, but reactivate more strongly owing to strong polarisation [19] and cathode reduction (becoming mixed conducting) as a consequence of underfed zones with lower oxygen partial pressure [10,18]. The process is repetitive as the cathode oxygen stoichiometry is reequilibrated upon cooling and load removal. Anode involvement is considered unlikely as no obvious anode mechanism is proposed which could be responsible for such repeated reactivation; the anode microstructure for sure changes at start-up (initial 24 h) but afterwards evolves in a single direction of performance degradation due to particle coarsening and spheridisation leading to triple phase boundary length reduction and loss of interconnectivity [20].

Fig. 9 illustrates that this reactivation phenomenon, again largely for the weakest border cell, is amplified after a few (three) thermal cycles. Fig. 9A, plotting the forward *i*–*V* scan taken after reaching 800 °C (fourth heating) and stable OCV at nominal gas flows, clearly demonstrates this different behaviour for cell 5. Fig. 9B shows, similar to Fig. 8C, the voltage re-increase on all cells (especially on cell 5) when imposing constant current of 0.4 and 0.46 A cm^{-2}, respectively. The different magnitude in transient response between Fig. 8C and Fig. 9B, after three thermal cycles, might be related to the onset of cathode delamination caused by cycling, reducing its active area but still carrying comparable total stack current. It may in addition be related to cathode densification, reducing the local PO_2 at the cathode–electrolyte interface. For both phenomena, the stronger polarised cathode is reduced more pronouncedly, leading to Sr surface segregation, more oxygen vacancy generation and stronger performance reactivation [19]. It is worth noting that the amount of reactivation follows roughly the sequence U1 < U2 < U3 < U4 < U5, i.e. from the first cell to be fed to the last in the stack. OCV values also confirm this tendency, with on average U1 showing highest and U5 lowest OCV (see further in Fig. 13A).

What is certainly evident from Figs. 8 and 9 is that a performance analysis based on *i*–*V* data taken at the beginning of each current load period would lead to misleading conclusions, and that instead those taken at the end of each polarisation phase, i.e. just before the next cooling, are more representative of the cell and stack potential.

Fig. 10 after 11 thermal cycles still reiterates the behaviour of Figs. 8 and 9, i.e. strong limitation on cell 5 at the beginning of repolarisation (12th heating) followed by important reactivation, the difference being, however, that overall performance has dropped, as evident from the polarisation current (right-hand side *Y*-axis), reaching only 0.3 A cm^{-2} since the 6th cycle (see also Fig. 7).

Indication of beginning cell failure is given in Fig. 11A: after 12 thermal cycles, during the 24 h current load period cell 3 degrades after only short reactivation (<10 h). At the beginning of the following cycle, the damage suffered by this cell is visible from its abnormal low OCV in the final *i*–*V* recording (1055 h) in Fig. 11B. End-of-life occurs shortly afterwards, Fig. 11C, with cell 3 collapsing to negative voltage.

Retracing the test history to try and identify where and why the stack failed, in particular because of cell 3, some anomaly was seen to occur already during the anode reduction in the start-up phase, Fig. 12. For about 15 min, a short circuit caused by a thermocouple lead labeled “T4” in the figure, occurred between cells 2, 3 and 4, with the voltage on cell 3 dropping to zero, before this was noted and corrected. Cell 5, consistently weakest in performance throughout the test, was in fact the fastest to reduce, and cell 3, causing eventual stack loss, indeed the slowest. Such difference in reduction speed may stem from misalignments in the stack assembly or from sealing defects, with inhomogeneous gas feed distribution

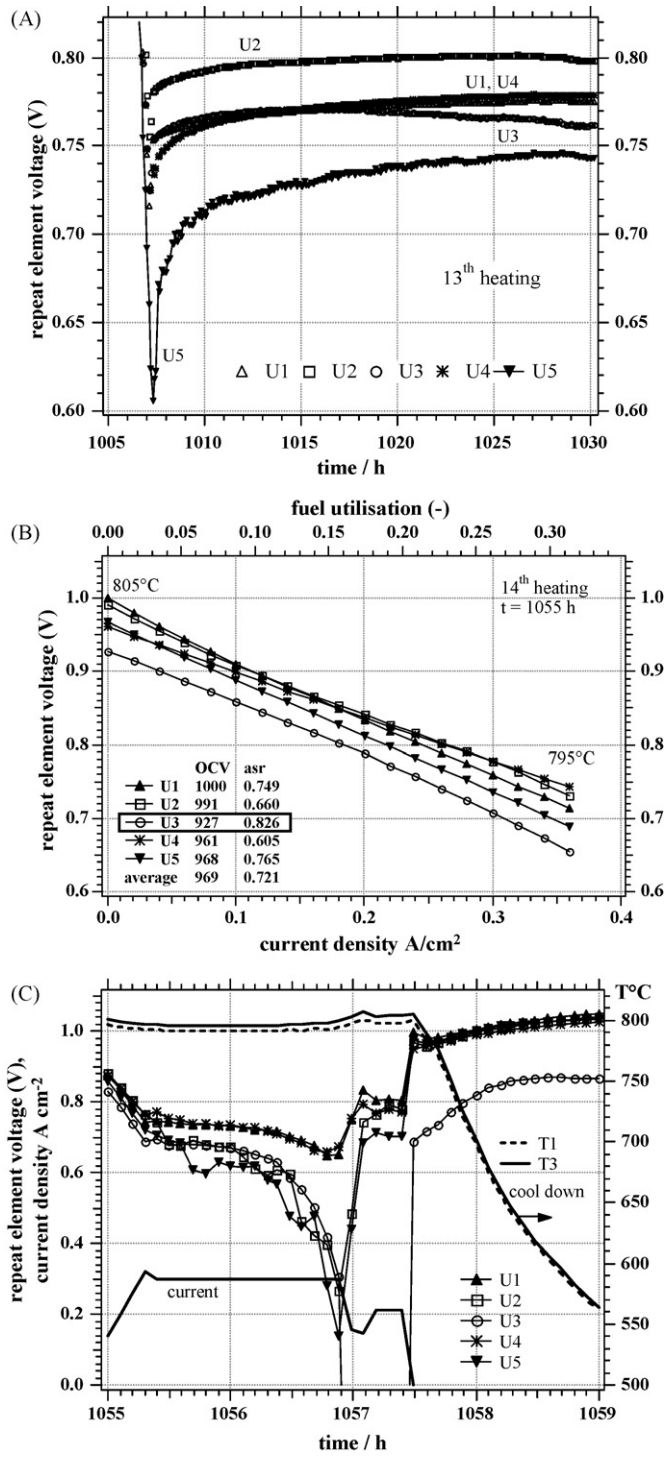

Fig. 11. (A) Voltage evolution with time at 0.3 A cm^{-2} stack current, following the forward *i–V* scan taken at 800 °C at the beginning of the 13th thermal cycle. The onset of degradation on cell 3 is clearly distinguished. (B) Current–voltage output of the 5-cell stack #3 after the 14th heating (13 thermal cycles), showing irreversible damage on the center cell 3, as a consequence of the degradation visible in (A). (C) Voltage evolution with time at 0.3 A cm^{-2} stack current, following the *i–V* scan taken in (B). The weakest cell 3 collapses to negative voltage, signing stack failure.

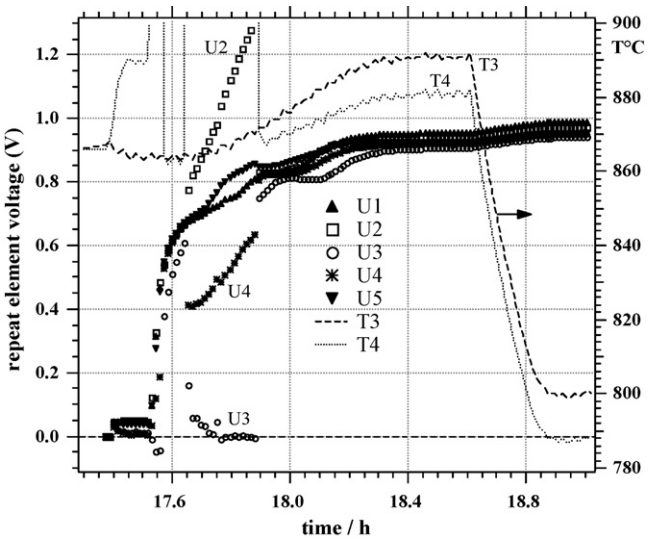

Fig. 12. Voltage evolution at start-up of 5-cell stack #3 during the anode reduction phase. Cells 2, 4 and especially cell 3 show anomalous values for ca. 20 min because of lead shorting via a thermocouple ("T4").

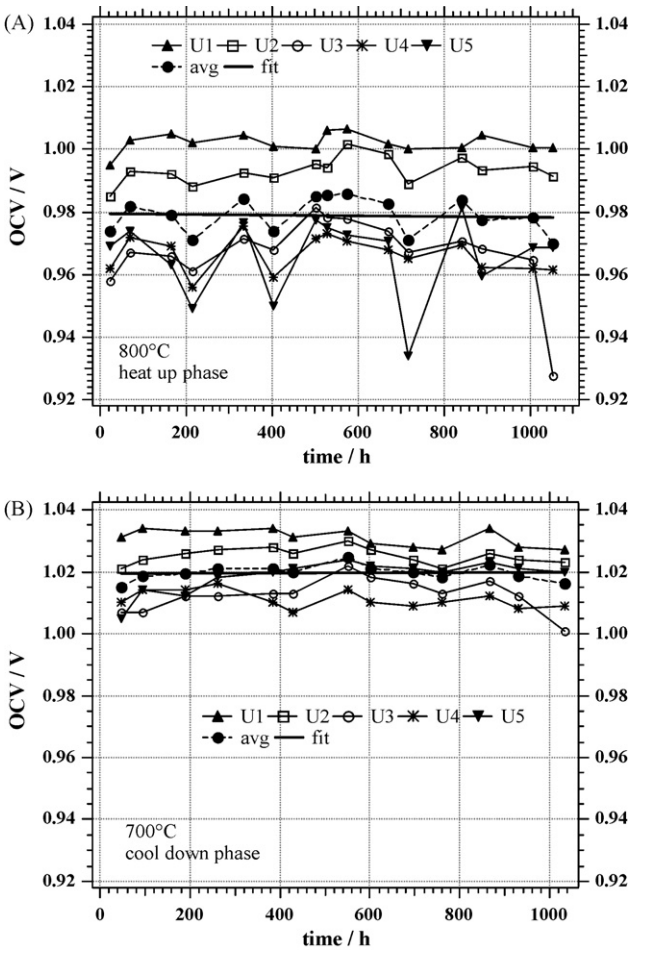

Fig. 13. (A and B) OCV on all cells of stack #3, at 800 °C (beginning of each load period, A), and at 700 °C (during cool down of each thermal cycle, B), until stack failure. OCV on average, though low, remains stable.

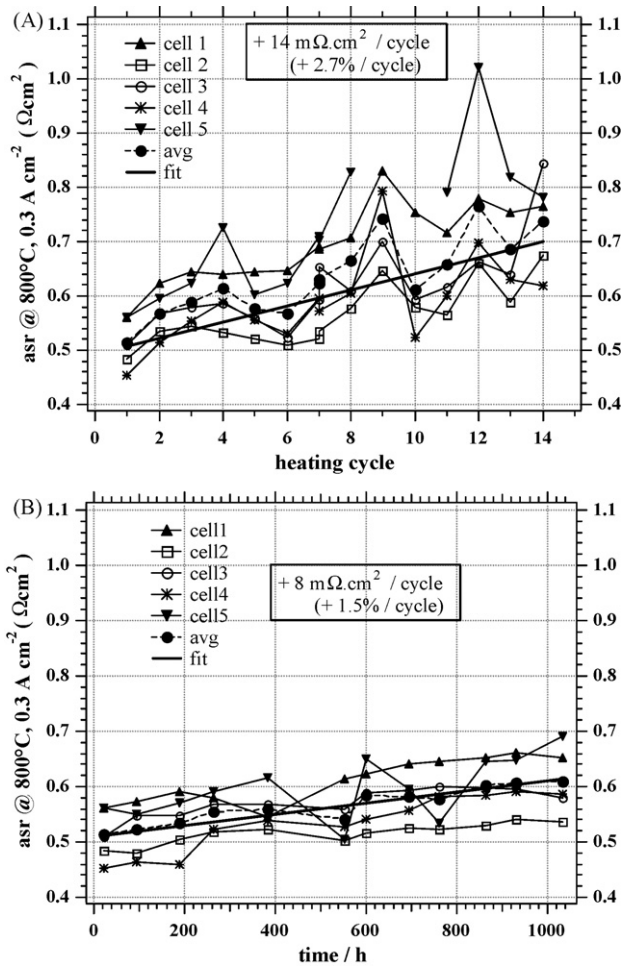

Fig. 14. (A and B) ASR at 800 °C and 0.2–0.3 A cm^{-2} for all cells of stack #3, for forward (A) and backward (B) *i*–*V* scan at beginning and end of each load period (see also Table 2). More reliable data is obtained from (B).

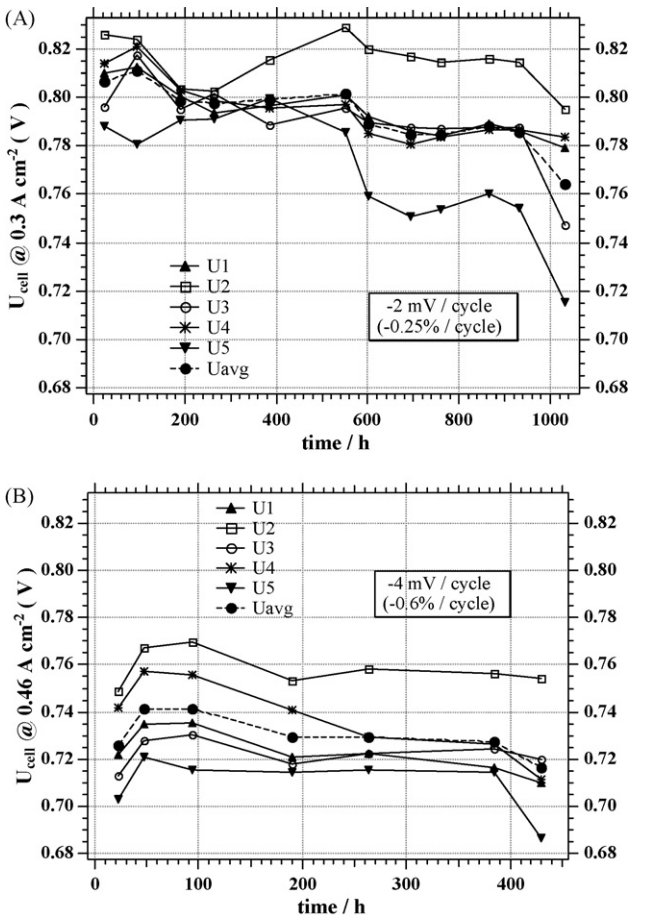

Fig. 15. (A and B) Steady-state voltage decay with time on all cells of stack #3 at 800 °C and 0.3 A cm^{-2} (A) and 0.46 A cm^{-2} (B), taken at the end of each load period (only until cycle 6 for 0.46 A cm^{-2}, see also Table 2). Relative degradation per thermal cycle, from these values, is lower than when expressed by ASR increase (Fig. 14).

over the different cells as a consequence [4,5]. Performance of cell 3 was always slightly below stack average, and the first to limit in the ASR vs. current density plot (see Fig. 8B), but this is easy to note with hindsight. It may be said that with growing testing experience and subtle observation, the weak spots in stacks (here the middle cell) can become detectable early in operation life. This is relevant for developing sensitive control strategies to extend stack lifetime.

Figs. 13–15 attempt to evaluate stack degradation quantitatively due to thermal cycling. First, it is mentioned that another 5-cell stack, identical to stack #3 here, had been operated before for 2700 h without thermal cycling [2,5,12], at 800 °C and 0.46 A cm^{-2} using the same gas flows as here, and that all cells slightly activated performance continuously over the first 1000 h before degradation set in (with −4% per 1000). Since the cumulated load time at 800 °C for the present stack was ca. 420 h (see Table 2), it may be assumed that the observed decay on stack #3 can be ascribed to the effect of thermal cycling essentially.

Fig. 13A shows cell OCV at 800 °C at the beginning of each current load period, i.e. after reaching 800 °C from the heat-up phases and at the start of current–voltage scanning. A few strong fluctuations are visible, in particular for cell 5. These could in part be due to insufficient stabilisation time before *i*–*V* recording (4th, 6th and 10th heating). Nevertheless, average OCV appears stable. More reliable data is obtained from Fig. 13B, displaying cell OCV values taken at 700 °C for each cool down phase, i.e. after the stack was polarised for at least 24 h and after current load had been removed for at least 1 h. Equally from this data it may be said that OCV seemed little affected by thermal cycling (Fig. 13A and B use same *Y*-scaling). It is remarked that OCV values at 800 °C were temperature corrected, for comparability between cycles. The highest measured temperature for each cycle varied between 801 and 810 °C at OCV (see Table 2), at 0.3 A cm^{-2} this was between 790 and 800 °C. The correction, using the Nernst equation, remained very small, though (1 mV (10 K)$^{-1}$).

Fig. 14, which plots ASR values to estimate the evolution of performance as a consequence of thermal cycling, illustrates how results may differ depending on the chosen data representation. As seen higher, Fig. 8B motivated why ASR values at 0.2–0.3 A cm^{-2} were determined; moreover, polarisation was limited to 0.3 A cm^{-2} after cycle 6 (Table 2, Fig. 7). Also for Fig. 14 a temperature correction was applied, so as to normalise all values to 800 °C, since a 10 K difference in temperature is not negligible for cell performance comparison. To this a straightforward Arrhenius relation was used, obtained from the independent test on the identical stack mentioned before [2,12], where *i*–*V* characteristics at the same flow were taken at 800, 750 and 700 °C. The ASR activation energy E_A between 800 and 750 °C amounted there to 42 kJ mol^{-1}; from formula (1), a 10 K difference thus shifted ASR values by up to 20–30 mΩ cm^2, or ca. 4% of the uncorrected ASR:

$$\mathrm{asr}(1073\,\mathrm{K}) = \mathrm{asr}(T)\exp\left(\frac{E_A}{R}\left(\frac{1}{1073}-\frac{1}{T}\right)\right) \quad (1)$$

where *R* is the ideal gas constant.

When calculating ASR values for all five cells from the *i*–*V* characteristics recorded just after each heating phase (i.e. forward-scan, see Table 2), the result in Fig. 14A is obtained. As we have seen that these *i*–*V* data are not constant (Figs. 8C, 9B, 10, 11A) and may strongly underestimate later performance after reactivation, fluctuations are important and average degradation, when derived from these data, overestimated to about 14 mΩ cm^2 loss in ASR (or +2.7%) per thermal cycle. If on the contrary the ASRs are evaluated from the backward *i*–*V* scans, after 20–24 h of polarisation and reaching more stable and improved performance, the result in Fig. 14B is obtained, showing with some exceptions a less fluctuating outcome but especially less effective degradation, namely 8 mΩ cm^2 loss in ASR per cycle or 1.5% per cycle (same *Y*-scaling is used in Fig. 14A and B).

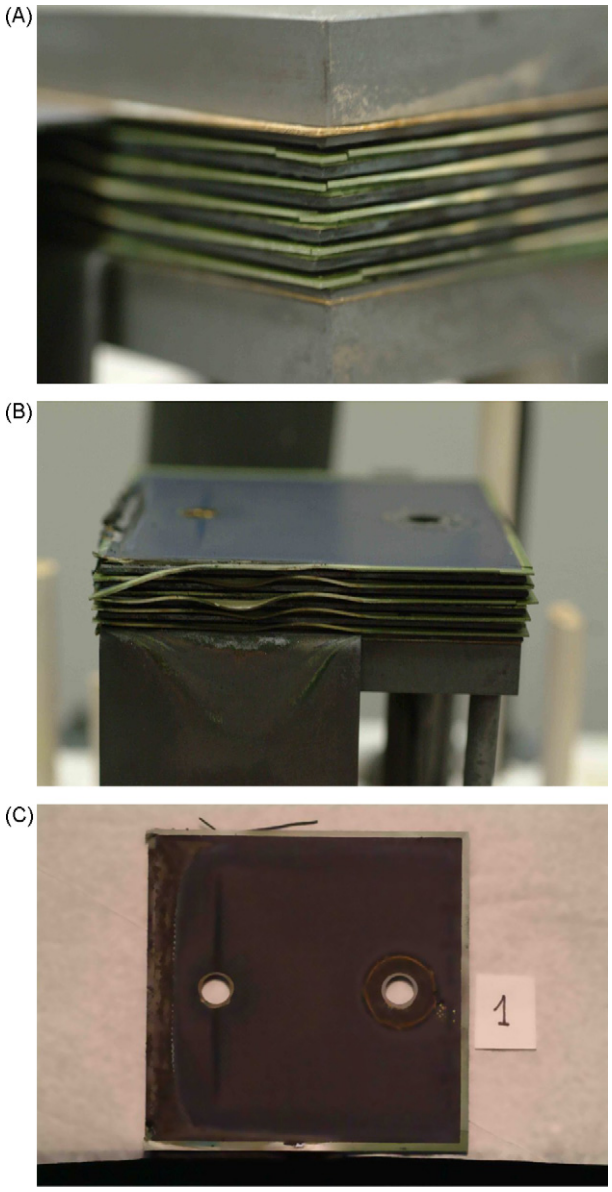

Fig. 16. (A–C) Stack #3 disassembly after 13 thermal cycles and failure on cells 3 and 5: (A) side view on fuel outlet, showing cracking of cells at the corners; (B) view on end-plate current collector side (see also Fig. 1), showing severe cell edge warping up to contact between cells 3 and 5; (C) top view on cathode of cell 1, showing serious damage closest to the fuel outlet (zone of uncontrolled post-combustion) up to cathode destruction, and therefore loss of active area.

Another, complementary, way of representing performance loss is given in Fig. 15, simply as the cell voltage at constant polarisation current after maximum stabilisation time (i.e. just before the backscan *i*–*V* and cool down phases); this could be done for 0.46 A cm^{-2} constant polarisation current up to six thermal cycles (first 400 h), and for 0.3 A cm^{-2} for all following cycles. For 0.3 A cm^{-2}, the corresponding cell voltages for the first 400 h were also plotted, from the backward scan *i*–*V* data. Again all values have been temperature corrected to normalise to 800 °C (formula (2)), using the temperature-corrected ASR values:

$$V(1073\,\mathrm{K}) = V(T) + j(\mathrm{asr}_T - \mathrm{asr}_{1073\,\mathrm{K}}) \quad (2)$$

where j is the current density (0.46 or 0.3 A cm^{-2}).

From this data treatment, one sees that mean cell voltage drops on average by ca. −4 mV per cycle (0.6%) and −2 mV per cycle (0.25%) for 0.46 and 0.3 A cm^{-2} current density operation, plotted in Fig. 15A and B, respectively, which is significantly less than the loss derived from ASR analysis (Fig. 14).

Observation of the disassembled stack gave a clear view on the reason of failure, as shown in Fig. 16. The stack and cell geometry are such that anode support edges are exposed to reduction–oxidation cycles, combined with excessive temperature due to uncontrolled post-combustion [2,5]. This has led to fissuring of the cells at the edges and corners (Fig. 16A), and extreme warping up to the point that cells 3 and 5 touch each other by a broken edge from the latter cell (Fig. 16B). This explains their anomalous behaviour towards the end-of-life of the stack, and their responsibility in final stack loss (Fig. 11). The top view on the cathode of for example cell 1, Fig. 16C (the outcome was very similar for all five cells), shows how active cathode area is lost at the fuel outlet (left), the cell edge where uncontrolled post-combustion takes place. The harsh conditions of high temperature, steam production and steam back-diffusion in this zone are such that the cathode is in part destroyed. This effect alone – an estimated loss in active area of roughly 5% – contributes to a large extent to the observed total degradation of ca. 20% (from ASR increase, Fig. 14B) or ca. 6% (from voltage decrease at 0.3 A cm^{-2}, Fig. 15A). However, in absolute terms, both expressions for performance loss correspond, with −2 mV cell voltage drop at 0.3 A cm^{-2} per cycle or 8 mΩ cm^2 ASR increase per cycle at 0.3 A cm^{-2} (i.e. −2.4 mV cell voltage drop).

The identical stack polarised for 2700 h under steady-state conditions (permanent 97% H_2 flow of 8 ml min^{-1} cm^{-2}) at 0.46 A cm^{-2} [2,12] degraded, after ca. 1000 h of slight activation, with about −4% per 1000 h (from voltage decay) and also showed cathode edge attack. Thermal cycling appears to aggravate overall performance loss because of sealing degradation and frequent gas flow changes (dilute fuel) during heating and cooling.

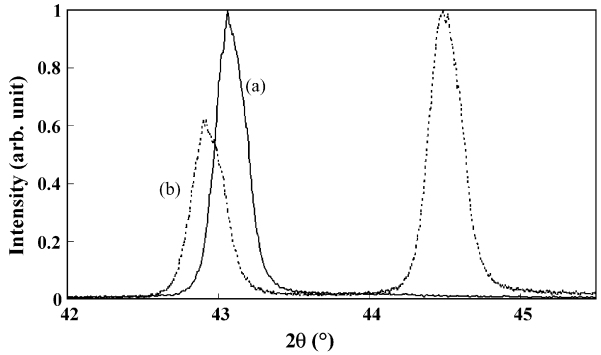

Fig. 17. XRD pattern of (Mg, Ni)O solid solutions using Cu Kα radiation. Solid line (a) shows as-synthesized sample and dotted line (b) shows the reduced sample. The reduction was carried out at 1000 °C in a mixture of 4 vol% hydrogen in nitrogen for 30 h.

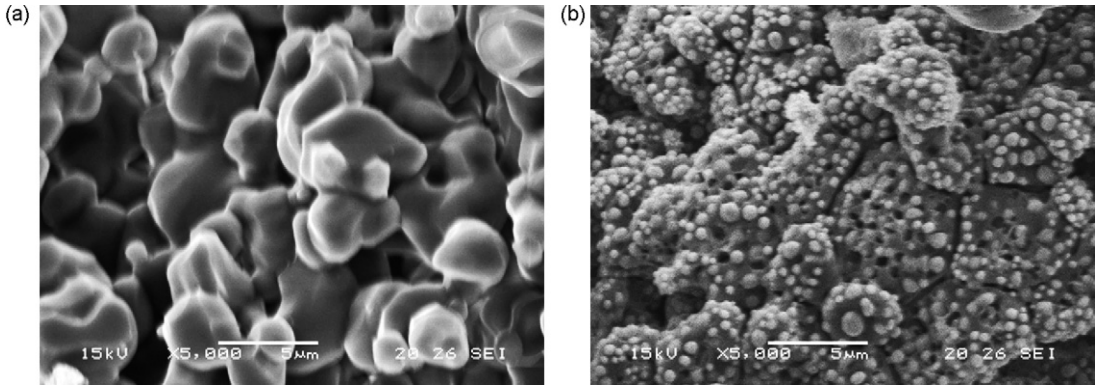

Fig. 18. SEM of fracture surfaces of (Mg, Ni)O solid solutions. Image (a) shows as-synthesized sample and image (b) shows the reduced sample. The reduction was carried out at 1000 °C in 4 vol% hydrogen in nitrogen (30 h).

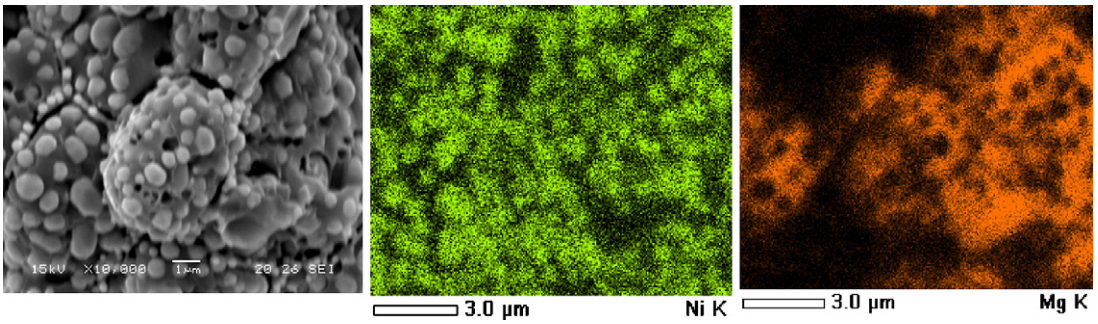

Fig. 19. SEM (left) and EDX mapping images (center and right) of the fracture surface of the (Mg, Ni)O solid solution after the reduction (1000 °C, 4 vol% H_2 in N_2 for 30 h).

The presented R-stack configuration having thus shown strong design limitation, here and elsewhere [3–5], a new stack configuration has been designed and validated [2,12], up to 72-cell stacks delivering >1 kW_{el}. Uncontrolled post-combustion at fuel outlet is avoided using fuel recovery, and leakages greatly reduced using hybrid sealing and a complete stack enclosure. All of these design measures strongly improve cell edge protection against reoxidation.

In parallel to design measures, intrinsic material development can help to improve the anode reoxidation tolerance. One such approach was explored by studying the expansion behaviour of MgO-added NiO.

3.3. MgO-added anode

(Mg, Ni)O solid solutions were synthesized, and the phase was analyzed by XRD. It was confirmed that single phase of (Mg, Ni)O solid solution existed in the samples as shown in Fig. 17a. The microstructure of the sample is shown in Fig. 18a, it consists of grains of approximately 2–5 μm in size.

(Mg, Ni)O solid solutions were reduced, and the phase was analyzed by XRD measurement. From the XRD profile as shown in Fig. 17b, the sample was analyzed to consist of (Mg, Ni)O solid solution and Ni metal. Because the position of the (2 0 0) line of the (Mg, Ni)O solid solution shifted close to that of MgO phase, the Ni content of the (Mg, Ni)O solid solution was considered to decrease. The microstructure of the sample is shown in Fig. 18b, with small particles of approximately 0.3–1.0 μm in size deposited on the (Mg, Ni)O solid solution. EDX analysis revealed that the small particles mainly consisted of Ni, as shown in Fig. 19. By the reduction of the (Mg, Ni)O solid solution, it is shown that small particles of Ni metal are segregated from the grains of the (Mg, Ni)O solid solution and deposited on it. The size of the sample was measured during the reduction, and the expansion profile shown in Fig. 20: the (Mg, Ni)O solid solution expands when it is reduced (Fig. 20), even if the total mass of sample is decreasing because some oxygen should leave. From these results, it is estimated that the expansion is possibly caused by the deposition of Ni particles between the (Mg, Ni)O grains and they enlarge the distance between the (Mg, Ni)O grains.

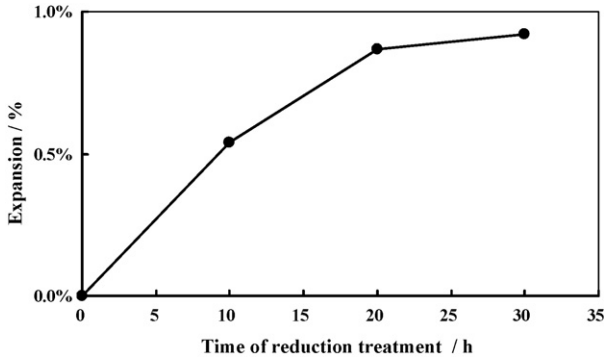

Fig. 20. Expansion behaviour of the (Mg, Ni)O solid solution by reduction treatment. The sample was reduced at 1000 °C in a gas mixture of 4 vol% hydrogen and nitrogen.

4. Conclusions

Two 5-cell stacks were tested for durability (800 °C), one with unprotected interconnects and operated for 2750 h at 0.35 A cm^{-2} current density (40% fuel utilization), showing ca. 6.7% per 1000 h voltage degradation. The second stack with coated interconnects showed an order of magnitude lower degradation rate of 0.83%

per 1000 h, operated at even higher fuel utilisation (60%) and current density of 0.5 A cm^{-2}. Even when different cell types (reputed intrinsically stable with <1% per 1000 h voltage loss) were used in both stacks, we believe this result indicates the effectiveness of the protective spinel layer against Cr poisoning.

A 5-cell stack was taken through 13 thermal cycles between 30–200 and 800 °C with current–voltage characteristics recorded at the beginning and end of typically 24 h constant current load periods. Average degradation was evaluated, as voltage decay at 0.3 A cm^{-2}, to −2 mV loss per thermal cycle, or as ASR increase at similar current density, to 8 mΩ cm^2 per cycle. Important transient behaviour was noted at the beginning of current load periods, as electrochemical cathode activation, especially on the border cell (no. 5) which was last to be fed. Stack loss after 1060 h and 13 cycles was due to the center cell (no. 3) and could be correlated to feed limitation on this cell and maybe to a short circuit occurring during the anode reduction phase at start up. Anode support reoxidation was severe on the cell edges causing warpage and fissuring.

The reduction behaviour of (Mg, Ni)O solid solutions was studied. When (Mg, Ni)O solid solutions were reduced at 1000 °C in a gas mixture of 4 vol% hydrogen and nitrogen, an expansion of the sample was observed. From the results of XRD and SEM/EDX analyses, the expansion mechanism is estimated to be caused by the segregation of Ni particles between (Mg, Ni)O grains and the resultant separation between grains.

Acknowledgements

The authors thank FZJ for the APS deposition of the protective coating on the CroFer 22 APU interconnects, as well as Energy Research Center Netherlands (ECN) and Haldor Topsø AS for for cell supply (ASC1, ASC2), finally the European Commission for financial support under the Real-SOFC contract SES6-CT2300-502612.

References

[1] D. Larrain, N. Autissier, F. Maréchal, J. Van herle, D. Favrat, J. Power Sources 131 (2004) 304–312.
[2] S. Diethelm, J. Van herle, Z. Wuillemin, A. Nakajo, N. Autissier, M. Molinelli, J. Fuel Cell Sci. Technol. 5 (2008) 007802.
[3] N. Autissier, D. Larrain, J. Van herle, D. Favrat, J. Power Sources 131 (2004) 313–319.
[4] J. Van herle, D. Larrain, N. Autissier, Z. Wuillemin, M. Molinelli, D. Favrat, J. Eur. Ceram. Soc. 25 (12) (2005) 2627–2632.
[5] Z. Wuillemin, N. Autissier, A. Nakajo, M.-T. Luong, J. Van herle, D. Favrat, J. Fuel Cell Sci. Technol. 5 (2008) 011016.
[6] V.R. Choudhary, A.M. Rajput, A.S. Mamman, J. Catal. 178 (1998) 576.
[7] H. Matsumoto, Shokubai 18 (1976) 71.
[8] E.P. Murray, T. Tsai, S.A. Barnett, Nature 400 (2000) 649.
[9] H. Ohta, S. Yamashita, T. Sobue, T. Seyama, Abstract of 31st International Cocoa Beach Conference & Exposition on Advanced Ceramics & Composites, 2007, p. 15.
[10] M. Molinelli, D. Larrain, N. Autissier, R. Ihringer, J. Sfeir, N. Badel, O. Bucheli, J. Van herle, J. Power Sources 154 (2) (2006) 394–403.
[11] M. Stanislowski, J. Froitzheim, L. Niewolak, W.J. Quadakkers, K. Hilpert, T. Markus, L. Singheiser, J. Power Sources 164 (2007) 578–589.
[12] O. Bucheli, M. Molinelli, T. Zähringer, E. Thorn, S. Diethelm, Z. Wuillemin, A. Nakajo, N. Autissier, J. Van herle, in: S. Singhal, H. Yokokawa (Eds.), Proceedings of the 10th International Symposium on SOFC, Electrochem. Soc. Inc., 65 South Main St., Pennington, NJ, USA, June 2007, Proceedings Volume 2007-7, pp. 123–133.
[13] N. Christiansen, J.B. Hansen, H. Holm-Larsen, S. Linderoth, P.H. Larsen, P.V. Henriksen, A. Hagen, ECS Trans. 7 (1) (2007) 31–38.
[14] http://www.hcstarck.de/medien/dokumente/document_flyer_ASC4_EN_102007web.pdf.
[15] J. Van herle, R. Ihringer, R. Vasquez, L. Constantin, O. Bucheli, J. Eur. Ceram. Soc. 21 (10-11) (2001) 1855–1859.
[16] D. Larrain, J. Van herle, F. Maréchal, D. Favrat, J. Power Sources 118 (2003) 367–374.
[17] A. Nakajo, C. Stiller, G. Härkegård, O. Bolland, J. Power Sources 158 (1) (2006) 287–294.
[18] M. Noponen, M. Halinen, J. Kiviaho, J. Saarinen, J. Fuel Cell Sci. Technol. 3 (4) (2006) 438–444.
[19] F.S. Baumann, J. Fleig, M. Konuma, U. Starke, H.U. Habermeier, J. Maier, J. Electrochem. Soc. 152 (10) (2005) A2074–A2079.
[20] D. Simwonis, F. Tietz, D. Stoever, Solid State Ionics 132 (2000) 241–251.